CFD Simulation and Robust Design Optimization of the Valve Seat and Orifice Plate in Port Fuel Injector

P. Daopiset[1], J. Bumrungpetch[2], E. Juntasaro[1] and A. Likitchatchawankun[1†]

[1] *Mechanical Engineering Simulation and Design Group, The Sirindhorn International Thai-German Graduate School of Engineering, King Mongkut's University of Technology North Bangkok. 1518 Pracharat 1 Road, Wongsawang, Bangsue, Bangkok 10800, Thailand*
[2] *Robert Bosch Automotive Technologies (Thailand) Co., Ltd. 7/102 Moo 4, Pluakdaeng, Rayong 21140, Thailand*

†*Corresponding Author Email: ampol.l@tggs.kmutnb.ac.th*

ABSTRACT

The mass flow rate of the fuel-air mixture can vary due to the geometry and dimensions of the valve seat and orifice plate at the tip of the port fuel injector. This study aims to reduce the standard deviation of the mass flow rate by optimizing four design parameters of the valve seat defined at the top (CHA1 – the angle between the valve seat and the bore wall and CHH1– its horizontal distance) and the bottom (CHA2 – the angle of the chamfer from the bottom of the valve seat and CHV2 – its vertical distance) of the edge breaks to guarantee a constant mass flow rate during its operation. The sensitivity analysis is implemented with the CFD simulation to generate the Design of Experiment (DOE) using ANSYS CFX and optiSLang. This created the correlation between design parameters and the averaged mass flow rate. The results indicate that CHA2 was the most impacting parameter on the mass flow rate. The Robust Design Optimization (RDO) is performed based on the Metamodel of Optimal Prognosis (MOP). Furthermore, the optimization loop processes the correlation function obtained from MOP using the Evolutionary Algorithms (EA) optimization method by keeping the standard deviation and the tolerance of the design parameters constant. In conclusion, the implemented EA optimization can reduce the standard deviation of the mass flow rate by approximate 51% and the new nominal designs at the valve seat edge breaks are obtained.

1. INTRODUCTION

The transportation technology has been significantly improved since the last century in terms of increasing engine efficiency and better output performance of the combustion engines (Yago, 1983; Reitz, 2013; Kalghatgi, 2015). To date, the majority of the automobile industries in the market use Internal Combustion (IC) engines as the main power supply (Smil, 2005). The first IC engine was successfully designed as a four-stroke engine by Otto in 1876 and the continuous development of the IC engine has been sustained since then (Raţiu, 2003; Smil, 2005). Within the worldwide automotive industry, the two most widely used injection systems in IC engines are Gasoline Direct Injection (GDI) system (Robert, 2022) and Port Fuel Injection (PFI) system, also called the manifold injection system (Golzari et al., 2016). The significant differences between GDI and PFI are the location of the injector and the operating pressure (Robert, 2022). Indeed, the GDI injector is directly installed inside the combustion

chamber, therefore, GDI injector requires a higher operating pressure compared to that of PFI injector locating in the intake manifold (Robert, 2022). For PFI system, the injected fuel flow was obstructed by a nozzle structure creating a pressure drop and the fluidic fuel turned into micro droplets with increasing total surface area (Schmidt et al., 1999). This atomization enhanced the mixing process of the fuel and the air in the intake manifold resulting in a better quality of exhaust with less emission as a result of complete combustion (Yang et al., 1993).

In the production development aspect, several prototypes of intake and exhaust parts including combustion chamber and injectors need to be designed, created, and tested in various experiments and under different working conditions consuming a large laboratory time and effort leading to unnecessary delay in the development and production processes. In addition, experimental measurement techniques are limited for such

Nomenclature				
P	pressure		**ABBREVIATION**	
$SS_E^{Prediction}$	sum of the squared prediction errors		ALHS	Advanced Latin Hypercube Sampling
SS_T	the equivalent of the total variation		CFD	Computational Fluid Dynamics
U, V, W	velocity in Cartesian's coordinate		CHA1	angle between the vertical bore wall and the valve seat wall
x, y, z	direction in Cartesian's coordinate		CHA2	angle of the bottom chamfer from the bottom of the valve seat
GREEK LETTER			CHH1	horizontal distance between the valve seat wall and the bore wall, μm
α_l	volume fraction of the liquid phase of a mixture		CHV2	vertical distance of the bottom chamfer from the bottom of the valve seat, μm
μ	dynamic viscosity of mixture phase		CoP	Coefficient of Prognosis
μ_{eff}	effective viscosity		DOE	Design of Experiment
μ_l	dynamic viscosity of liquid phase,		EA	Evolutionary Algorithm
μ_t	turbulent dynamic viscosity		GDI	Gasoline Direct Injection
μ_v	dynamic viscosity of vapor phase		HPC	High Performance Computing
ρ	density of mixture phase		IC	Internal Combustion
ρ_l	density of liquid phase		MassFlow Avg	averaged mass flow rate
ρ_v	density of vapor phase		MassFlowr ateStddev	standard deviation of the averaged mass flow rate
SUBSCRIPT AND SUPERSCRIPT				MOP
E	error of the prediction value		OVAT	One Variable at A Time
l	liquid phase		RDO	Robust Design Optimization
Prediction	prediction value		Re	Reynolds number
T	total variation		SI	Spark Ignition
t	turbulent		y_1^+	first layer mesh height adjacent to the wall
v	vapor phase			

a complex geometry of spark ignition (SI) system composed of various components resulting in immense difficulty in obtaining a comprehensive information in flow physics, in most cases nearly impossible (Alam et al., 2020). Thanks to fully-developed computational software, such prototype models can be designed and created in a simulation software within hours to represent their actual models being tested under various test conditions and its measurement data could be precisely chosen from the simulation domain for further analysis and optimization (Relich, 2016).

The conventional method used to determine the most suitable design was the One Variable at A Time (OVAT) method (Czitrom, 1999). This OVAT method calculates only one parameter while holding other parameters constant (Bora et al., 2022). Indeed, the input parameters having less impact on the output responses will be automatically ignored by the OVAT method (Czitrom, 1999; Bora et al., 2022). Hence, the evaluation of the outputs obtained from the OVAT method could lead up to uncertainty and often incorrect results for the further optimization process (Czitrom, 1999). To overcome this problem, the Design of Experiment (DOE) was introduced in which even the less impacting parameters are also taken into account (Antony, 2023). This DOE analysis was implemented in this study to find the impact of each design parameter on the averaged mass flow rate of the fuel-air two-phase mixture in some initial design cases and in the further optimization process.

2. BACKGROUND

On the one hand, several numerical researches on PFI system with their experimental model validation mainly focuses on (i) the design improvement of one or more components in PFI system to enhance engine performance and/or functionality requirements (Cecere et al., 2023; Rashid et al., 2024), (ii) the 3D computational simulation of the intake port with combustion chamber and/or exhaust port as a whole under specific conditions and various key performance parameters to improve the performance and efficiency (Pan et al., 2014; Baratta et al., 2021; Sahoo & Srivastava, 2023; Bellis et al., 2024), (iii) using CFD simulation for a specific purposes, i.e., to compare performance and emission characteristics in spark ignitions (Bhaduri & Mallikarjuna, 2023; Gammaidoni et al., 2024; Singh et al., 2024) or to only investigate spray characteristic in IC engines (Zoumpourlos et al., 2023), and (iv) CFD simulation exclusively for PFI injector part to investigate a simplified plume spray model using AVL FIRE CFD software (Anekwanna & Juntasaro, 2018). Therefore, only few studies using CFD simulation for PFI injector are, to some degrees, relevant to this present research paper and its scope of the investigation. On the other hand, several researches on GDI injector demonstrate greater relevance to this present parametric study and DOE analysis of PFI injector valve seat (Hellmann et al., 2017; 2018; Biçer & Yurtkuran, 2020).

Hellmann et al. (2017) studied a high-pressure Gasoline Direct Injection (GDI) injector with four design parameters. Their CFD simulation indicated that the optimal atomization of the fuel can be achieved by increasing the turbulent kinetic energy owing to low spray hole conicity, smaller opening spray hole angle, and the larger spray hole length. More recently, Hellmann et al. (2018) also predicted the nozzle flow and the spray characteristics with the different geometry parameters of the GDI injector valve seat using the CFD-workflow coupling transient Eulerian nozzle flow with transient Euler-Lagrange spray simulations and experimentally validated their CFD simulation using the two-hole injectors with predetermined design parameters. Moreover, their DOE analysis with 700 of the 3D-CFD designs were evaluated (Hellmann et al., 2018).

In 2020, Biçer and Yurtkuran studied the flow inside a GDI Injector and parameterized the pressure of the system and a few geometric design parameters such as pitch circle diameter (CD), angle of the nozzle (I-angle), and conicity for different physical fuel types to investigate the impact on spray angle and cavitation formation using CFD simulation and DOE analysis (Biçer & Yurtkuran, 2020). The result showed that the pitch circle diameter affected the spray angle significantly and the angle of the nozzle influenced the wall-wetting condition while fuel type was the most influential parameter for the cavitation inception (Biçer & Yurtkuran, 2020).

Previous parametric studies and DOE analysis focused mainly on investigating the injector tip with a round shape located in the GDI while the investigation of the valve seat in PFI injector has not been much studied yet. (Hellmann et al., 2017; 2018; Biçer & Yurtkuran, 2020). This present study investigates various geometries of the valve seat defined by four main design parameters in the PFI injector using CFD simulation, DOE analysis, and a robust design optimization process. The investigated actual PFI injector has been researched in Robert Bosch Automotive Technologies (Thailand) Co., Ltd. facility and it needs to be improved, developed, and optimized. This parametric study is applied to the valve seat model at its top and bottom edges. The four design parameters considered are (i) the angle between the valve seat and the bore wall at the top edge break, CHA1 and (ii) its horizontal distance, CHH1 as well as (iii) the angle of the bottom chamfer from the bottom of the valve seat, CHA2 and (iv) its vertical distance, CHV2. Here, the CFD simulation is performed using ANSYS CFX 2022R2 and the Design of Experiment (DOE) analysis method is implemented for this parametric study. Furthermore, the sensitivity analysis method is used to explore the impact of each parameter on the averaged mass flow rate obtained from CFD simulation results. Finally, the robust design optimization process using ANSYS optiSLang analyzes all the designs and selects the best design with the minimum standard deviation of the averaged mass flow rate of the fuel-air two-phase mixture. These optimal design parameters obtained from CFD simulation and ANSYS optiSLang may well be further investigated for the production of the actual valve seat in this given working condition.

3. NUMERICAL METHODOLOGY

3.1 Governing Equations

In this study, the governing equations of the two-phase flow of a fuel-air mixture are considered. The Reynolds-Averaged Navier-Stokes (RANS) equations are coupled with the turbulence two-equation eddy viscosity model (Giancarlo, 2009). In addition, the two-phase mixture with the homogeneous equilibrium model is used under the assumption of the completely mixed liquid and vapor phases, such that, the velocity, pressure, and temperature are equal in both phases (Clerc, 2000).

The 3D continuity equation of a steady two-phase mixture flow can be written in a differential form as (Yusuf et al., 2020),

$$\frac{\partial (\rho U_j)}{\partial x_j} = 0. \tag{1}$$

Similarly, the 3D momentum equation of a steady two-phase mixture flow can be written in a differential form as (Serra, 2023),

$$\frac{\partial (\rho U_i U_j)}{\partial x_j} = -\frac{\partial P}{\partial x_i} + \frac{\partial}{\partial x_j}\left[\mu_{eff}\left(\frac{\partial U_i}{\partial x_j}\right)\right], \tag{2}$$

$$\mu_{eff} = \mu + \mu_t, \tag{3}$$

where ρ is the previously defined two-phase mixture density in Eq. (1) and μ_{eff} is the effective viscosity. Here, μ_t is the turbulent viscosity defined in accordance with the selected turbulence model (Serra, 2023). Moreover, P is the thermodynamic pressure, U_i refers to the velocity components (U, V, W), and x_i denotes the Cartesian coordinates (x,y,z).

3.2 Two-Phase Mixture Properties

The density ρ and viscosity μ of the mixture of the steady two-phase flow are calculated in the phase change based on the volume fraction of the liquid phase α_l, (Nouri-Borujerdi & Kebriaee, 2012)

$$\rho = (1 - \alpha_l)\rho_v + \alpha_l \rho_l \tag{4}$$

$$\mu = (1 - \alpha_l)\mu_v + \alpha_l \mu_l \tag{5}$$

where ρ_v, ρ_l, μ_v, and μ_l are the density and the dynamic viscosity of the vapor and liquid phases, respectively.

3.3 Turbulence Modeling

Considering the fluid flow direction in the orifice plate with the circular redirection passage, the fluid flow is expected to create a swirl. This swirl, in turn, increases some degree of turbulence and the complexity of the fluid flow. Therefore, the near-wall fluid flow region needs to be carefully investigated. Besides, the flow inside the valve seat and orifice plate channel also requires a thorough examination due to the wall curvature design of the orifice plate affecting the averaged mass flow rate.

Several well-established turbulence models were built into CFD simulation software for various applications and purposes (Giancarlo, 2009). Each turbulence model has its advantages and disadvantages depending on factors such

as Reynolds number, wall treatment, and flow behavior (Clerc, 2000; Giancarlo, 2009; Yusuf et al., 2020). The most well-known turbulence model is the two-equation eddy viscosity model and it requires two transport equations (Menter, 1994; Bredberg, 2001). Furthermore, the commonly used two-equation turbulence models are k-ε and k-ω models (Giancarlo, 2009). On the one hand, the k-ε turbulence model is suitable for the free shear flow with a high Reynolds number while it cannot accurately capture the physics of the near-wall flow (Mohammadi & Pironneau, 1993). On the other hand, the k-ω turbulence model is more suitable for the near-wall region and the separation zone of the fluid flow with a low Reynolds number (Mohammadi & Pironneau, 1993; Wilcox, 2008).

To overcome these limitations, Menter et al. (2020) developed a new turbulence model called the Generalized k-ω (GEKO) turbulence model. The GEKO model shows high adaptability of following the flow behavior by changing the six free parameters without impacting the flat plate boundary layer flow. The GEKO model equations are showed in Appendix I.

3.4 Parametric Study

One of the most commonly used strategies for the design exploration, especially for nonlinear and stochastic systems, is metamodeling (Booker et al., 1999). In a metamodeling or surrogate model, the surrogate function of the output response is represented by the model input, for instance, Polynomial regression and Kriging (Most & Will, 2008). However, a vast number of samplings are required in multi-dimensional problems leading to the challenges in the sampling generation process (Most & Will, 2011). The Metamodel of Optimal Prognosis (MOP) was developed by Dynardo in 2008 to improve the optimal filter configurations generally lacking in the previous metamodels (Most & Will, 2010).

In this parametric study, the DOE approach and the MOP are implemented to identify the impact of the design parameters on the averaged mass flow rate. In general, the Coefficient of Prognosis (CoP) is used to determine the correlations between each input parameter and the output response (Most & Will, 2008). In this study, CoP is implemented to indicate the influence of the four design parameters as the inputs on the averaged mass flow rate as the output. Then, the parameter that correlates the most with the output is considered as the highest impact on the response (Most & Will, 2008). The prognosis of the forecast quality needs to be evaluated by using a test data set (Mohammadi & Pironneau, 1993). The relation between the metamodel assessment and the real test data can be expressed as (Most & Will, 2008),

$$CoP = 100 \times \left(1 - \frac{SS_E^{Prediction}}{SS_T}\right) \qquad (6)$$

where $SS_E^{Prediction}$ and SS_T are the sum of squared prediction errors and the equivalent of the total variation, respectively.

3.5 Single-Objective Optimization

In a general optimization process, a single scalar value of an objective function formulation is typically defined as (Ansys, 2022),

$$f(x_1, x_2, \ldots, x_k) \to min \qquad (7)$$

where $f(x_1, x_2, \ldots, x_k)$ is the function of the design variables x_k. The design variables could possibly be continuous with the lower and upper bounds or discontinuous with various discrete values (Ansys, 2022). One of the most popular and widely used single-objective optimization methods since past two decades is Evolutionary Algorithm (EA) population-based method due to its ability in solving complex problems in optimization process (Vikhar, 2016; Ansys, 2022). The Evolutionary Algorithm (EA) is the stochastic search inspired by the nature behavior of selection (Holland, 1992). This algorithm was created by Holland (1992) with the curiosity regarding work of nature adaptation, mutation, and selection to an environment (Holland, 1992; Bäck & Schwefel, 1993; Vikhar, 2016). In this study, the single-objective optimization with Evolutionary Algorithm (EA) was implemented into ANSYS optiSLang to evaluate the set of design parameters with the minimal standard deviation in averaged mass flow rate.

4. GEOMETRY AND COMPUTATIONAL DOMAIN

4.1 Geometry of the Valve Seat and Orifice Plate

Figure 1(a) shows a full 3D conical-shaped valve seat located at the top of the multi-hole orifice plate consisting of four outlet holes investigated in this study. This CFD was precisely created in consistent with an actual valve seat and orifice plate models and their corresponding geometry and application. First, the orifice plate model was obtained by 3D scanning of an actual production sample produced by stamping method. Then, the valve seat model was created according to the prototype drawings. In addition, the definitions and the ranges of the four design parameters shown in Table 2 were licensed by Robert Bosch Automotive Technologies (Thailand) Co., Ltd. Furthermore, both valve seat and orifice plate domains are combined and defined as one domain of interest. However, the tremendous size of this full 3D simulation domain leads to high computational cost and power requirements. Taking advantage of the symmetrical conditions, the full model is divided into four identical sub-domains and only one-fourth of the full 3D model is used in the CFD simulation as shown in Fig. 1(b). Here, Fig. 1(c) indicates the locations of the four design parameters, namely CHA1, CHH1, CHA2, and CHV2 at the valve seat domain of simulation with their corresponding range values listed in Table 1.

4.2 Boundary Conditions

Figure 1(d) presents the named selections of each boundary condition in the simulation domain specified according to the Port Fuel Injection (PFI) actual working conditions by Robert Bosch Automotive Technologies (Thailand) Co,. Ltd. The boundary conditions are specified as follows:
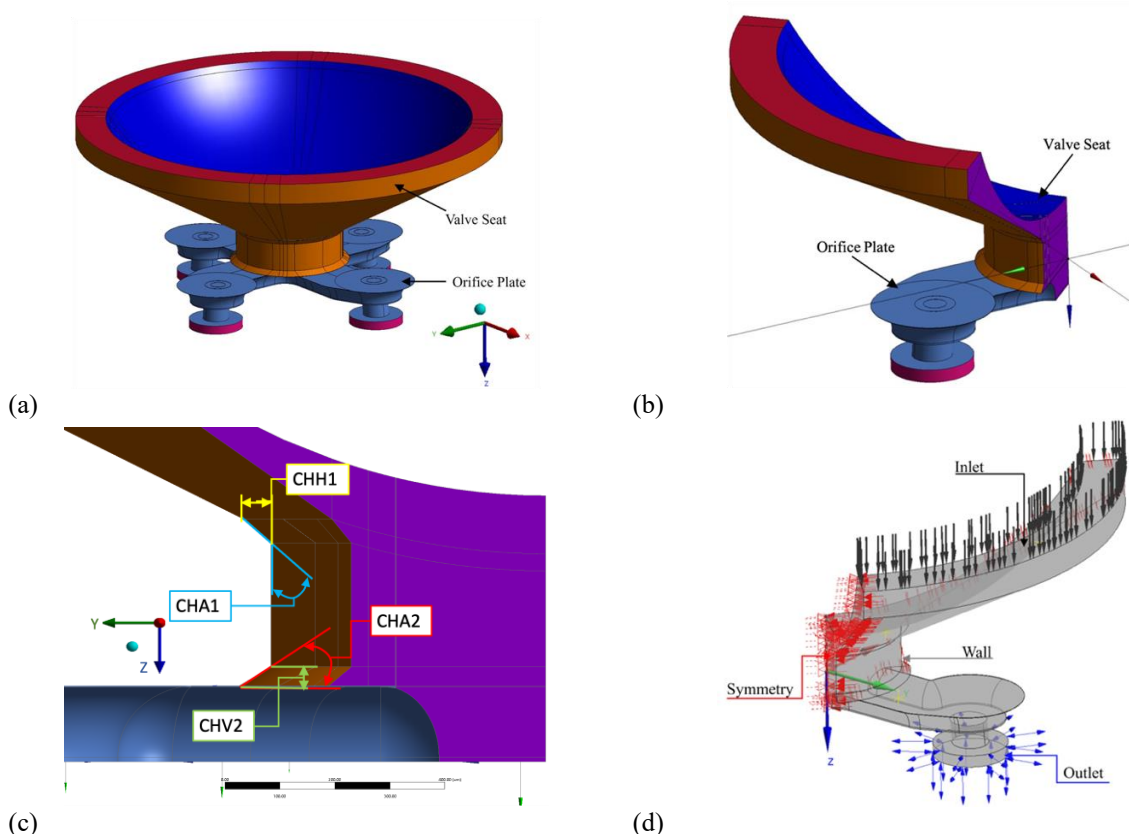
(a)

(b)

(c)

(d)

Fig. 1 (a) Complete 3D full model of the valve seat and orifice plate, (b) Its one-fourth model, (c) The locations of the four design parameters CHA1, CHH1, CHA2, and CHV2 with their corresponding possible ranges listed in Table 2, and (d) The boundary conditions of the valve seat and orifice plate: inlet, outlet, wall, and symmetry condition

Table 1 Definition and simulation ranges of the four design parameters, CHA1, CHH1, CHA2, and CHV2

Parameter	Definition	Minimum value	Maximum value
CHA1	The angle between the vertical bore wall and the valve seat wall	5°	58°
CHH1	The horizontal distance between the valve seat wall and the bore wall	10 μm	200 μm
CHA2	The angle of the bottom chamfer from the bottom of the valve seat	5°	85°
CHV2	The vertical distance of the bottom chamfer from the bottom of the valve seat	5 μm	120 μm

Table 2 Fluid properties of air and n-Heptane. (Sagdeev et al., 2013; Ghasemi et al., 2017)

Fluid	Density (kg/m^3)	Dynamic viscosity (kg/m·s)
Air (25 °C) (Ghasemi et al., 2017)	1.185	1.831 x 10^{-5}
n-Heptane (Sagdeev et al., 2013)	684.0	4.172 x 10^{-4}

- Inlet condition: Inlet pressure (P_{in}) constant at 4 bar

- Outlet condition: Outlet pressure (P_{back}) constant at 1 bar

- Side wall conditions: Symmetrical planes

- Walls of valve seat and orifice plate: Stationary walls with no-slip conditions.

Note that this CFD model is modeled under the assumption of an adiabatic system, therefore, the heat transfer that may arise from entropy of mixing and/or drag friction or the heat transfer from or to the surrounding was not considered.

The steady state CFD simulation runs 3500 iterations for each design of the total of forty-nine designs and the arithmetic average of the mass flow rate is calculated using the data of the last 1000 iterations as the result converges and reaches steady state condition. The convergence criteria were set up using relative residuals within the limit of $1.0x10^{-5}$ for all equations (continuity, x-momentum, y-momentum, z-momentum, k-equation, and ω-equation). The High-Performance Computing (HPC) is utilized to carry out the CFD simulation with forty-two processor cores in parallel for each case.

In an actual working scenario of PFI, the n-Heptane specified as a primary fluid and air as a secondary fluid are
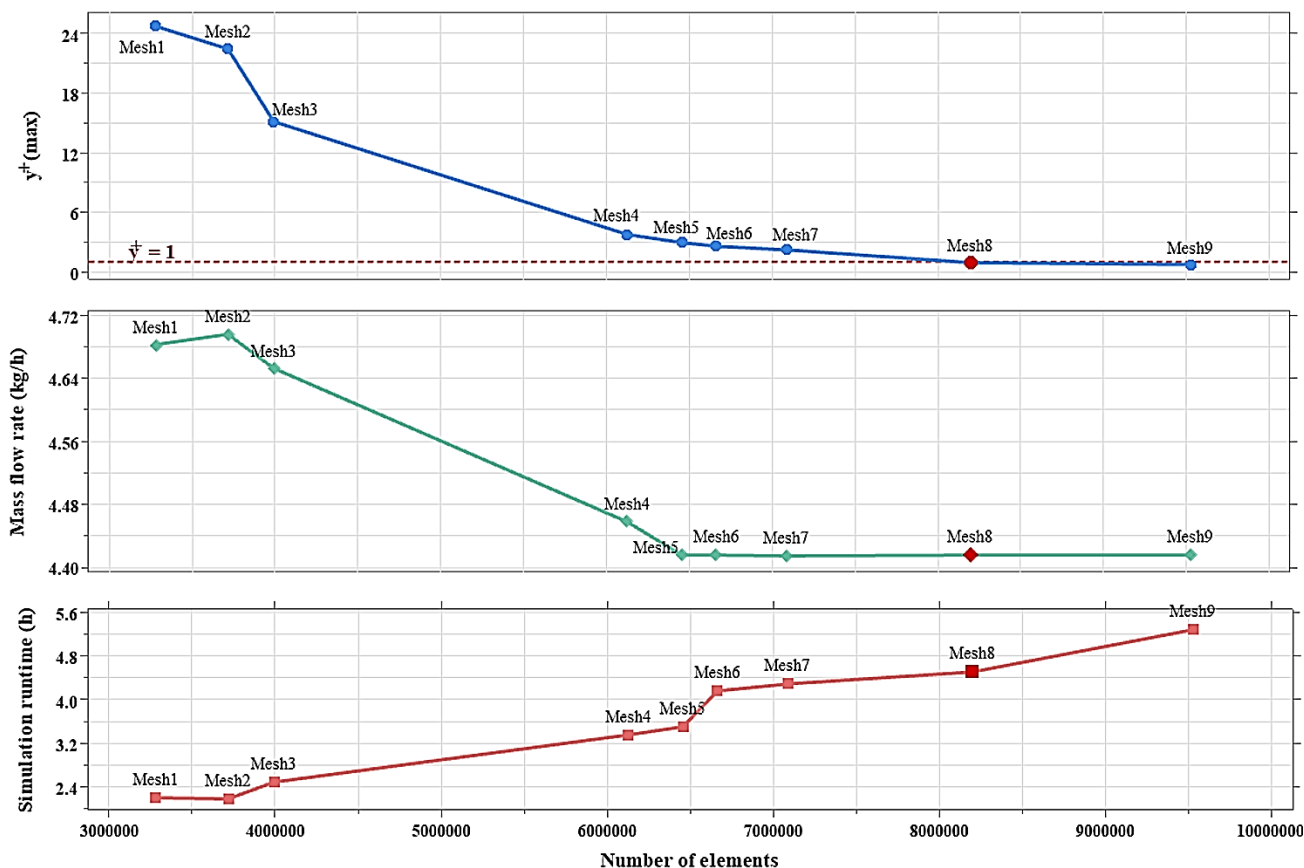
Fig. 2 The plots of y_1^+ maximum, mass flow rate (kg/h), and simulation runtime (h) as functions of the number of elements for nine cases in mesh-independent study

homogeneously mixed (Hinckel et al., 2008; Forte et al., 2012; Wang et al., 2016; Maio et al., 2022). The densities and viscosities of n-Heptane and air at 25°C are shown in Table 2.

5. MESH INDEPENDENT STUDY

The mesh-independent study was initially conducted to ensure the reliable simulation results regardless of the size and the number of mesh. Figure 2 shows the nine cases of mesh-independent investigation with various first inflation layer heights y^+ and the associated number of mesh elements compared in terms of the averaged mass flow rate and the maximum value of the first y^+, denoted as y_1^+, adjacent to the wall. The x-axis indicates the number of elements and the y-axis indicates the y_1^+ maximum value, the averaged mass flow rate, and the CFD simulation runtime. The growth rate is using 10 % with all cases. The results from Mesh 1 to Mesh 4 reveal the significant variation of the averaged mass flow rate depending on the number of the mesh elements. The averaged mass flow rates become fairly constant from Mesh 5 to Mesh 9. However, the maximum y_1^+ needs also to be considered in addition to the mass flow rate. According to the k-ω turbulence model family, the near-wall region within the viscous sublayer requires precise investigation. Indeed, the y_1^+ maximum value should be less than 1 for properly capturing the near-wall fluid behavior (Salim & Cheong, 2009). The maximum value of

the y_1^+ starts becoming less than 1 in Mesh 8, therefore, Mesh 8 shown in Fig. 2 is selected for further simulation. Here, Mesh 9 is also suitable for the simulation, however, Mesh 9 contains about 1.3 million more elements (≈16% more mesh elements) compared to Mesh 8 resulting also in about 0.8 h longer simulation runtime for each case (see Table 3). The selected mesh is shown in Fig. 3. The mesh quality is shown in Table 4 which is considered the criteria according to the ANSYS CFX.

6. RESULT AND DISCUSSION

6.1 CFD Simulation Results

All forty-nine designs with varying dimensions of valve seat top and bottom edges are simulated using ANSYS CFX powered by HPC. Figure 4 presents 3 representative results showing that the flow experiences the first variation in geometry at the top edge of the valve seat defined by CHA1 and CHH1. At this top edge, the flow tends to detach from the tilting wall due to the fact that the vectors in velocity gradient cannot follow the abrupt geometry change of the wall plane and the flow then reattaches to the vertical wall again before experiencing another variation at the bottom edge of the valve seat. The bottom edge geometry defined by CHA2 and CHV2 also induces the flow to separate from the wall leading to the thicker near-wall separation zone. To clearly illustrate and assess these separation zones, three

(a)   (b)
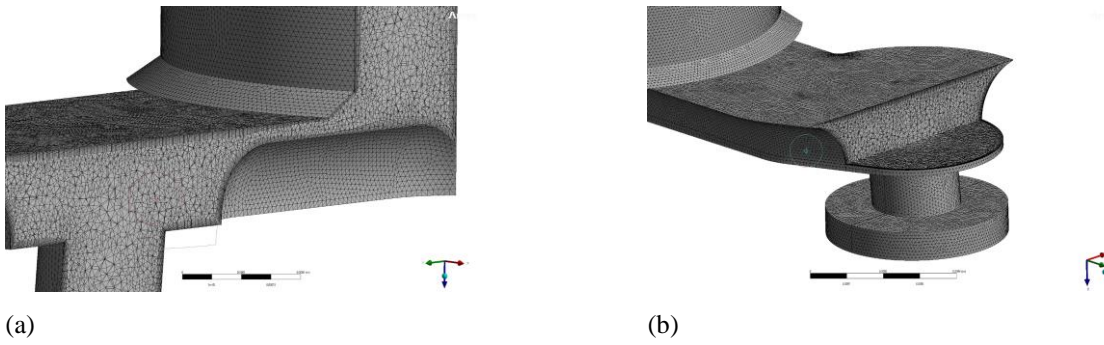
Fig. 3 Zoomed-in view of computational mesh structure and mesh distribution for Mesh 8 after the mesh-independent study: (a) The cut-through side view of the valve seat and orifice plate and (b) A cut-through side view at the swirl chamber of the orifice plate

Table 3 Mesh independent investigation of the number of elements and the first inflation layer height comparing with y_1^+ maximum, averaged mass flow rate (kg/h), and the CFD simulation runtime

Case	First inflation layer height (μm)	Number of elements	y_1^+ maximum	Averaged mass flow rate (kg/h)	CFD simulation runtime (h)
Mesh 1	9.00	3,278,851	24.69	4.682	2.19
Mesh 2	8.00	3,715,208	22.41	4.695	2.17
Mesh 3	5.00	3,992,371	15.10	4.652	2.48
Mesh 4	1.00	6,124,668	3.75	4.458	3.35
Mesh 5	0.80	6,454,086	2.94	4.682	3.50
Mesh 6	0.70	6,661,062	2.57	4.695	4.16
Mesh 7	0.50	7,088,047	2.20	4.652	4.29
Mesh 8	0.20	8,197,041	0.92	4.458	4.51
Mesh 9	0.18	9,526,846	0.73	4.458	5.29

Table 4 Mesh quality for selected Mesh (Mesh 8)

	Orthogonal Quality	Skewness	Aspect Ratio
Min	0.10050	0.00000	1.15780
Max	0.99928	0.89995	53.16400
Average	0.77932	0.21882	4.60670

Table 5 Geometry comparison between the three representative design points 20, 17, and 28 in term of the averaged mass flow rate (MassFlowAvg)

Design Point	CHA1 (°)	CHH1 (μm)	CHA2 (°)	CHV2 (μm)	MassFlowAvg (kg/h)
20	44.49	24.25	84.60	46.98	4.393
17	25.02	162.95	66.20	60.78	4.416
28	56.68	187.65	53.40	97.58	4.433

representative cases from all forty-nine cases with significant differences among them were selected to explain the flow behavior.

Figure 4 shows the three cases of the Design Points (a) 20, (b) 17, and (c) 28 with varying four design parameters at the top and bottom edges listed in Table 5. All three cases exhibit the separation zone around the top edge of the valve seat caused by the sharp edge indicated by the large value of CHA1. In Design Point 17 with the smallest CHA1 and the least sharpened edge, the fluid flow is smoother, hence, smaller separation zone compared to one of the Design Point 20. Then, the flow can reattach itself onto the surface further down along the streamline due to

turbulence overcoming adverse pressure gradient. In addition, at the bottom edge variation defined by CHA2 and CHV2, the flow also reveals the effect of the drastic geometry change resulting in significant differences in the separation zone thickness among the three cases. Design Point 20 [Fig. 4(a)] contains the smallest vertical distance CHV2 = 46.98 μm and the largest bottom chamfer edge angle CHA2 = 84.60° characterizing a short perpendicular wall connecting to the orifice plate. This nearly perpendicular wall forces the fluid to flow around the sharp edge resulting in a large separation zone. The reduction in the bottom chamfer edge angle to a smaller value of CHA2 = 66.20° in Design Point 17 [Fig. 4(b)] leads to a smoother transition in geometry and in fluid

(a) Design Point 20 (CHA1 = 44.49°, CHH1 = 24.25 μm, CHA2 = 84.60°, and CHV2 = 46.98 μm)

(b) Design Point 17 (CHA1 = 25.02°, CHH1 = 162.95 μm, CHA2 = 66.20°, and CHV2 = 60.78 μm)

(c) Design Point 28 (CHA1 = 56.68°, CHH1 = 187.65 μm, CHA2 = 53.40°, and CHV2 = 97.58 μm)
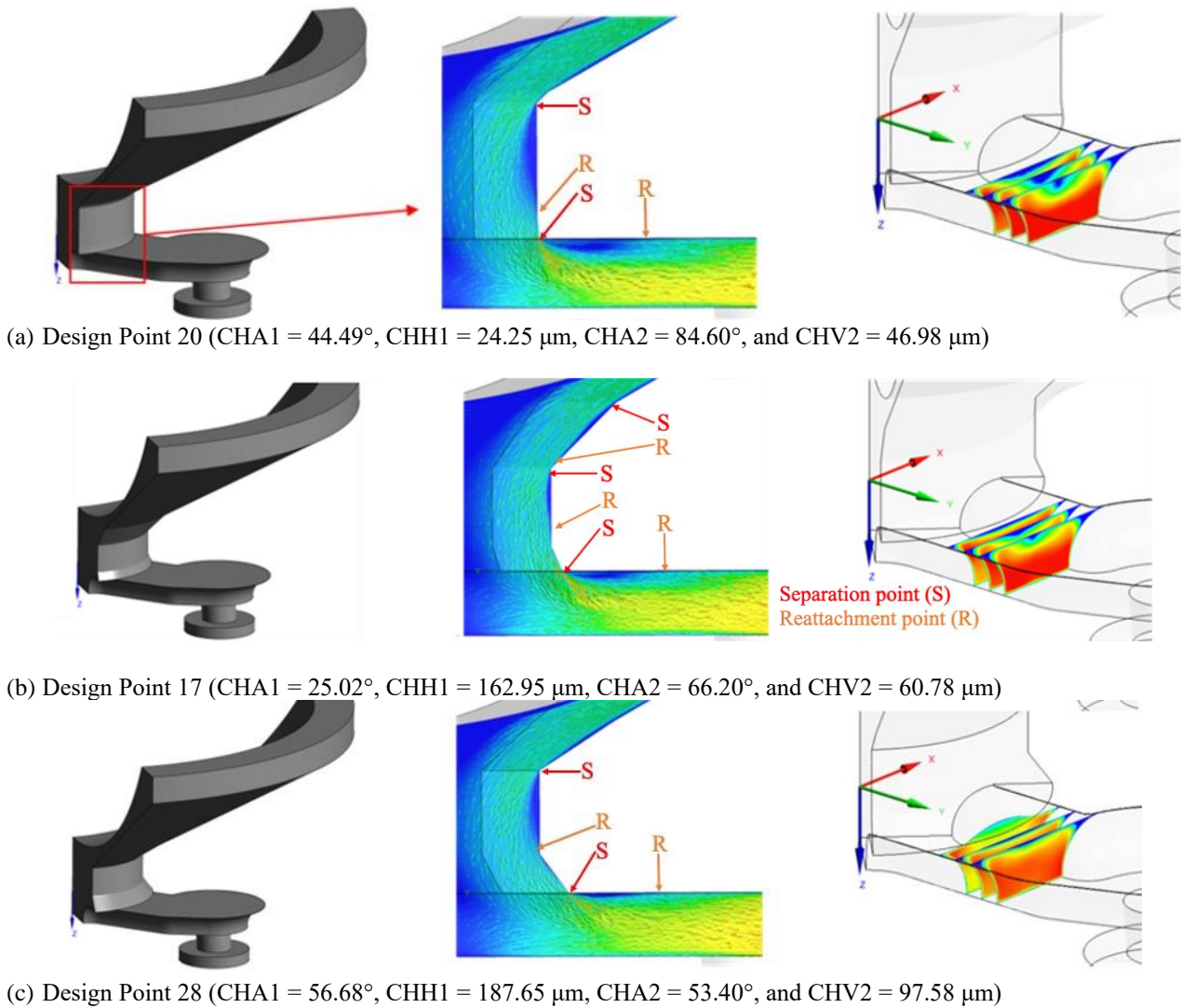
Fig. 4 Velocity contours of the two-phase mixture fluid flow in the YZ plane in the middle sub-figures and in the XZ plane in the right sub-figures of the Design Points (a) 20, (b) 17, and (c) 28 according to their geometry in Table 5

flow behavior compared to Design Point 20, hence, the reduction of the separation zone thickness. Moreover, Design Point 28 [Fig. 4(c)] with the smallest bottom chamfer edge angle CHA2 = 53.40° in combination with the largest vertical distance CHV2 = 97.58 μm diminishes the separation zone substantially.

Figure 4 also shows the effective fluid flow areas in three cross-section XZ planes for y = 550 μm, 610 μm, and 670 μm insides the orifice plate channel as consequences of the separation zone caused by the flow coming from the valve seat bottom edge. For Design Point 20 [Fig. 4(a)], the largest separation zone impedes the fluid flow and the effective flow area is reduced, hence, the smallest averaged mass flow rate as presented in Table 5. In other words, the reduction in the separation zone thickness increases the effective flow area, and thus, the highest averaged mass flow rate as demonstrated by Design Point 28.

In this present study, however, the standard deviation of the averaged mass flow rate is a more important aspect

than the flow rate value itself. The reason is that a numerical and actual model should operate with high reliability and produce a constant mass flow rate of the fuel-air mixture with the least standard deviation. Hence, the stability of mass flow rate becomes the first priority and maintaining its minimal standard deviation that may arise from design tolerance in the production and from changes in working conditions is a more significant consideration. Therefore, all initial CFD simulation results are subjected to further sensitivity analysis and the robust design optimization.

6.2 Sensitivity Analysis

First, the quality of the metamodel needs to be evaluated for its reliability and the trustworthiness of the results. In ANSYS optiSLang, the quality of the metamodel can be described and evaluated using Coefficients of Prognosis (CoP) given in Eq. 18. Figure 5 shows the CoP of MOP from all forty-nine designs. Here, the CoP = 81% indicates a good prediction quality in
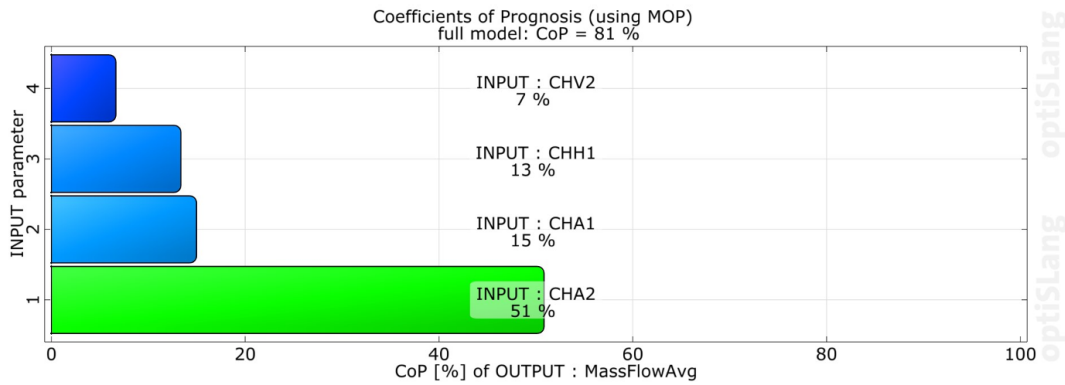
Fig. 5 Coefficients of Prognosis (CoP) indicating the impact of four input design parameters, CHA1, CHH1, CHA2, and CHV2 on the averaged mass flow rate (MassFlowAvg)

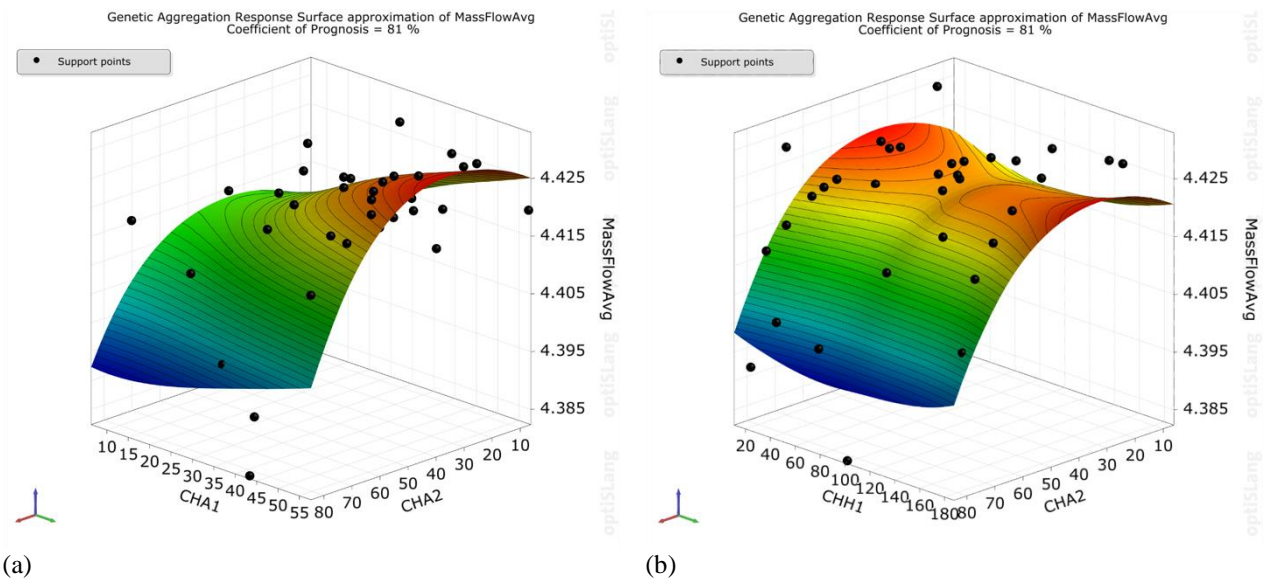(a)   (b)

Fig. 6 The 3D surface function of the averaged mass flow rate (in kg/h) as a function of a design parameter pair (a) CHA1 (in °) and CHA2 (in °) and (b) CHH1 (in μm) and CHA2 (in °)

consistent with the previous studies (Most & Will, 2008; Ptchelintsev et al., 2010). In addition, the most significant design parameter is CHA2 with CoP = 51% while CHA1, CHH1, and CHV2 are of inferior importance indicated by CoP = 15% for CHA1, CoP = 13% for CHH1, and CoP = 7% for CHV2. The MOP also confirms that changing in CHA2 largely affect the separation flow behavior and the effective flow area leading to the varying mass flow rate.

Furthermore, the CFD simulation results of all forty-nine designs were evaluated and the averaged mass flow rate of each design was plotted against a pair of design parameters, CHA1 and CHA2 in Fig. 6(a) and CHH1 and CHA2 in Fig. 6(b). The 3D surface plots in Fig. 6(a) and 6(b) show regression approximation of all forty-nine data points with the CoP = 81%. The color on the surface plots indicates the value of the averaged mass flow rate with red representing highest value while blue indicating the smallest value of the averaged mass flow rate. The tendency on the surface plot in Fig. 6(a) shows that the designs with high mass flow rate density populate where CHA1 is large and CHA2 is small. Figure 6(b) also represents the trend of the high mass flow rate being denser when CHA2 is small, however, it did not show a

clear trend of CHH1 impacting the averaged mass flow rate unlike that of the design parameter CHA1 in Fig. 6(a) as the CoP of CHH1 shows less impact compared to CHA1 as previously shown in Fig. 5. Additionally, 3D surface functions of Figs. 6(a) and 6(b) and their corresponding specific function expressions for each fitted surface as an approximation obtained by using MATLAB are shown in Appendix II.

6.3 Robust Design Optimization

Figure 7 shows the workflow diagram of Robust Design Optimization (RDO) in ANSYS optiSLang. First, the tolerance and the standard deviation of the four design parameters extracted from the measured data shown in Table 6 are sent to the optimization process as initial values of the nominal design. In general, the optimization concept is to shift the nominal value of all design parameters to obtain the minimum possible standard deviation of the mass flow rate by keeping the tolerance and the standard deviation of the design parameters constant. In this study, one hundred samplings are created randomly by varying four design parameters within a robustness evaluation loop using the Advanced Latin Hypercube Sampling (ALHS) method corresponding to
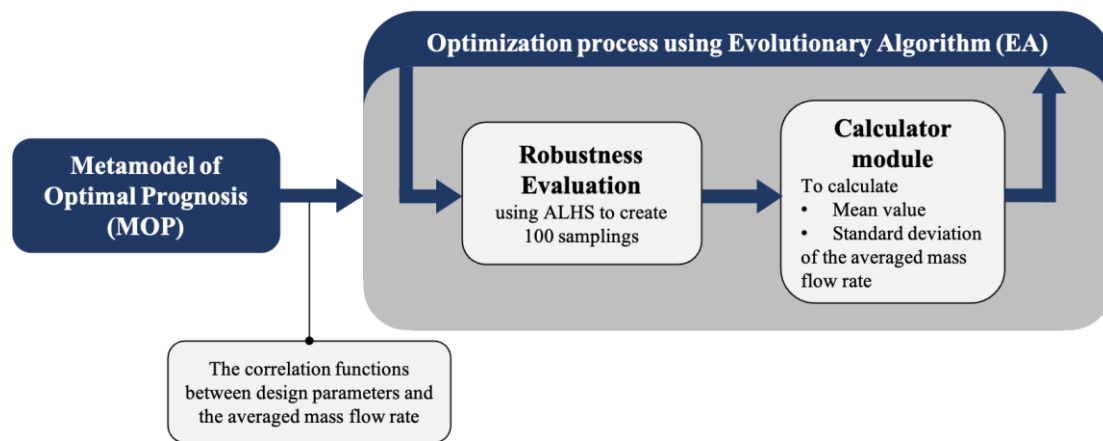
Fig. 7 Schematic diagram of the Robust Design Optimization (RDO) in ANSYS optiSLang consisting of Metamodel of Optimal Prognosis (MOP) and the optimization unit composed of a Robustness Evaluation and Calculator module

Table 6 Design parameter within their acceptable ranges, tolerances, and the standard deviations of the design parameters according to the drawings of CHA1, CHH1, CHA2, and CHV2

Parameter	Minimum value	Maximum value	Mean value	Tolerance of the design parameters	Standard deviation of the design parameters
CHA1 (°)	39.7	43.3	41.5	±3.68	1.83
CHH1 (μm)	52.7	131.0	94.4	±36.6	17.9
CHA2 (°)	20.0	70.0	45.0	±20.0	6.67
CHV2 (μm)	20.0	100.0	60.0	±20.0	6.67

the previous MOP within its lower and upper bounds of the measured data listed in Table 6. Once the one hundred samplings were generated, the calculator module calculates the mean value and the standard deviation of the averaged mass flow rate. These two values are sent to the optimization loop as the first nominal design. After the first nominal design is optimized, the new nominal design parameters are obtained and this new nominal design and its associated new set of design parameters are sent to the robustness loop again. The optimization process repeats itself in iterations until the minimum standard deviation of the averaged mass flow rate is obtained. In this investigation, the population-based Evolutionary Algorithms (EA) is used for the optimization process. This EA optimization process runs up to in a total of 500 iterations to ensure that the optimized design is achieved and converged.

Figure 8 shows the history line of the standard deviation of the averaged mass flow rate (MassFlowRateStddev) in an EA optimization process. The green dots represent all design points in the EA optimization process while the blue line indicates the convergence line of the EA optimization process detecting some minimal values of the standard deviation becoming smaller. From the first to about the fiftieth iteration, the optimized design in progress does not yet converge and shows a high standard deviation of the averaged mass flow rate. Subsequently, the standard deviation of the mass flow rate steadily reduces in the successive iterations along the convergence line. Eventually, the minimum standard deviation of the averaged mass flow rate is found in the

Design #301 out of 500 designs. Further down the EA optimization process from Design #301, the optimizer tries to reach the even lower value of the standard deviation of the mass flow rate, but the rest of the generated designs does not lead to any change of the fitness function, therefore, the optimizer concludes the Design 301 as the best design with the minimum standard deviation of the averaged mass flow rate.

Figure 9 shows the 3D plots of the standard deviation of the averaged mass flow rate (MassFlowRateStddev) versus design parameters of (a) CHH1 and CHA1 and (b) CHV2 and CHA2. The low-population area within the 3D plot indicates the initial phase of the EA optimization process as some nominal designs have not been yet optimized. By contrast, the high density of the design point population in a specific area translates to the optimized value of the standard deviation as each design point moves closer to the target value step by step. Eventually, the minimum standard deviation of the averaged mass flow rate is found in Design #301 with its design parameters.

Figure 10(a) depicts the standard deviation of the averaged mass flow rate in the so-called Best Design #301 before and after the EA optimization process. The result shows that the standard deviation of the optimized design can be reduced from the initial design by approximate 51% from 1.98×10^{-3} to 9.14×10^{-4}. Each design parameter was also optimized and the new design parameters are obtained in Fig. 10(b) with CHA1 = 39.7°, CHH1 = 88.1 μm, CHA2 = 28.8°, and CHV2 = 28.6 μm. is found in Design #301
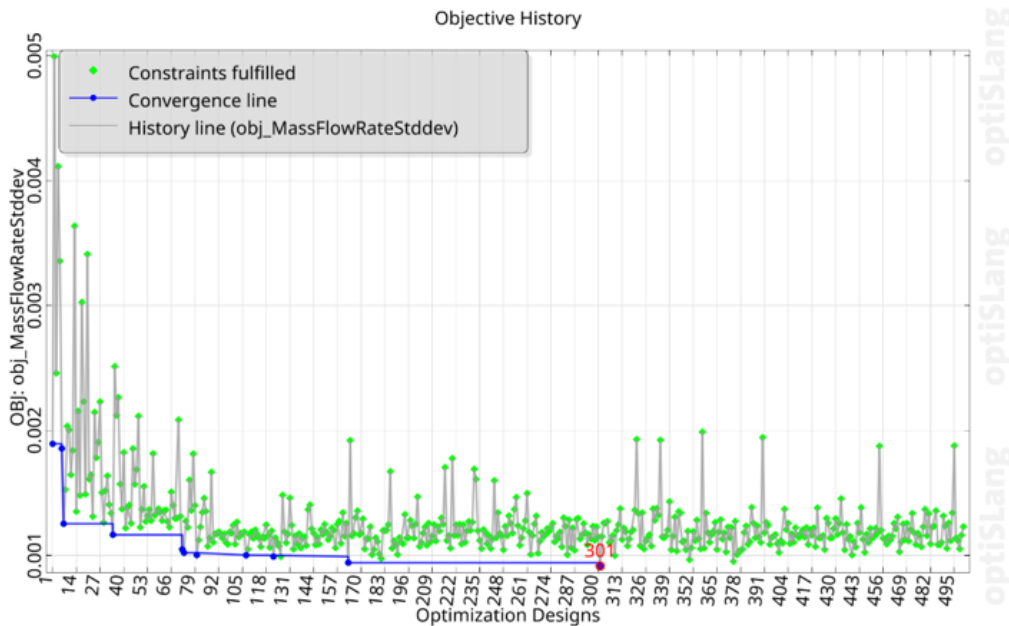
Fig. 8 Sequential history line (in gray) of the standard deviation of the averaged mass flow rate as a function of the 100 randomly generated design points fulfilling the geometric constraints (green dot) in each optimization step for 500 steps in including the convergence line (in blue) detecting successive decreasing in the standard deviation of the averaged mass flow rate
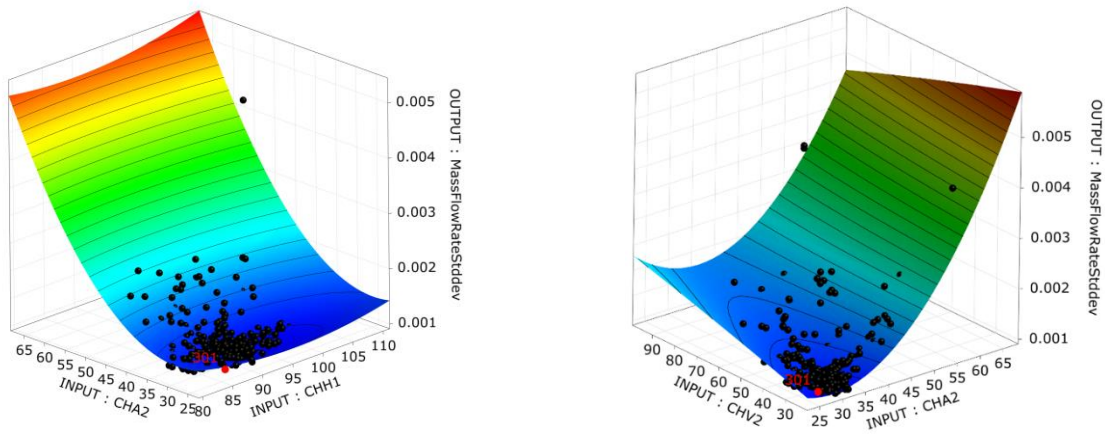

(a)   (b)

Fig. 9 The 3D surface function of the standard deviation of the averaged mass flow rate (in kg/h) as a function of a design parameter pair (a) CHH1 (in µm) and CHA1 (in °) at the top edge as well as (b) CHV2 (in µm) and CHA2 (in °) at the bottom edge. The so-called Best Design #301 found in the optimization process in Fig. 8 also marked as the minimum value corresponding to the four optimized design parameters

(a)   (b)
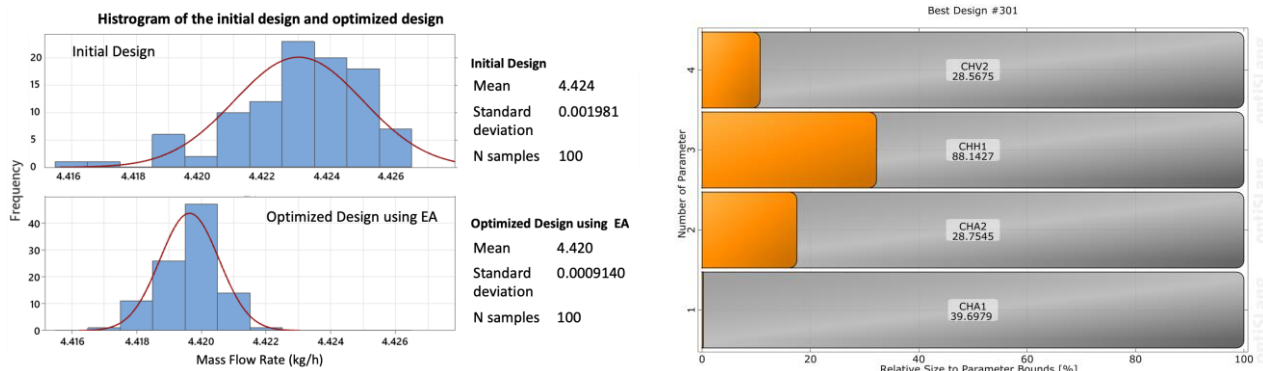
Fig. 9 (a) Mass flow rate distributions of the initial design with nominal design parameters and the optimized design and (b) The value of each design parameter of the robust design (the Best Design #301) after the EA optimization process

with its design parameters. Furthermore, 3D surface function of Figs. 9(a) and 9(b) and their corresponding specific function expressions are also shown in Appendix II.

7. CONCLUSION

This parametric study on the valve seat and the orifice plate in Port Fuel Injection (PFI) injector investigates four design parameters at the top and bottom edges of the valve seat. The forty-nine designs were generated based on the Design of Experiment (DOE) analysis. First, each of these forty-nine designs was simulated using ANSYS CFX with imposed boundary conditions of 4 bar inlet pressure at the top of the valve seat and 1 bar outlet pressure at the flow outlet of the orifice plate. In addition, to study the turbulent flow of the two-phase, fuel-air mixture generated by PFI injector, the Reynolds-Averaged Navier-Stokes (RANS) equations coupled with the Generalized k-ω (GEKO) turbulence model were used for calculation. Furthermore, a mesh independent study was conducted to ensure the accuracy of the simulation results and the optimal mesh regarding its size, number of elements, and the first layer mesh height adjacent to the wall was successfully identified. Second, the simulation results of all forty-nine designs show some degree of separation zone occurring around the top edge as well as the bottom edge of the valve seat depending mainly on the geometry defined by the four design parameters, namely (i) CHA1, the angle between the vertical bore wall and the valve seat wall, (ii) CHH1, the horizontal distance between the valve seat wall and the bore wall at the top edge, (iii) CHA2, the angle of the bottom chamfer from the bottom of the valve seat, and (iv) CHV2, the vertical distance of the bottom chamfer from the bottom of the valve seat. Three representative cases out of forty-nine designs with distinctive wall geometry were studied and compared in term of the averaged mass flow rate. At the top edge of the valve seat, the smaller value of CHA1 indicates the lesser sharp top edge leading to a smoother fluid flow with smaller separation zone. At the bottom edge of the valve seat, the smallest CHV2 combined with the largest CHA2 characterizes the sharpest bottom edge resulting in the largest separation zone. Overall, large separation zone obstructs the fluid flow and reduces the averaged mass flow rate. According to Coefficient of Prognosis (CoP) using Metamodel of Optimal Prognosis (MOP), the design parameter CHA2 shows the highest impact on the averaged mass flow rate. Finally, for the stability consideration in actual application requiring constant mass flow rate, the minimal standard deviation of the mass flow rate is desirable. The Robust Design Optimization (RDO) in ANSYS optiSLang using Evolutionary Algorithm (EA) optimization process investigates one hundred design samples randomly generated by Advanced Latin Hypercube Samplings (ALHS) and identifies the so-called best model with the least standard deviation of the averaged mass flow rate.

CONFLICT OF INTEREST

The authors declare no conflict of interests relating to the presented work.

AUTHORS CONTRIBUTION

Pornteera Daopiset: Conceptualization, Data curation, Formal analysis, Investigation, Methodology, Software, Validation, Visualization, Writing – original draft, Writing – review & editing. **Jeerasit Bumringpetch**: Conceptualization, Methodology, Resources. **Ekachai Juntasaro**: Formal analysis, Supervision, Writing – review & editing. **Ampol Likitchatchawankun**: Conceptualization, Formal analysis, Investigation, Project administration, Supervision, Validation, Writing – original draft, Writing – review & editing.

REFERENCES

Alam, A., Mittal, M., & Lakshminarasimhan, V. (2020). *Analysis of in-cylinder flow and cycle-to-cycle flow variations in a small spark-ignition engine at different throttle openings*. SAE Technical Paper. https://doi.org/10.4271/2020-01-0793

Anekwanna, C., & Juntasaro, E. (2018, December 11-14). *Model assessment of a single plume spray injector in dynamic PFI engine simulation*. The 9th TSME International Conference on Mechanical Engineering. TSME ICoME, Phuket, Thailand.

Ansys optiSLang. (2022). *Methods for Multi-Disciplinary Optimization and Robustness Analysis.* ANSYS Inc.

Antony, J. (2023). *Design of experiments for engineers and scientists.* Elsevier.

Bäck, T., & Schwefel, H. P. (1993). An overview of evolutionary algorithms for parameter optimization. *Evolutionary Computation, 1*(1), 1-23. https://doi.org/10.1162/evco.1993.1.1.1

Baratta, M., Misul, D., & Xu, J. (2021). Development and application of a method for characterizing mixture formation in a port-injection natural gas engine.

Energy Conversion and Management, 227, 113595. https://doi.org/10.1016/j.enconman.2020.113595

Bellis, D. V., Piras, M., Bozza, F., Malfi, E., Novella, R., Gomez-Soriano, J., & Olcina-Girona, M. (2024). Development and validation of a phenomenological model for hydrogen fueled PFI internal combustion engines considering Thermo-Diffusive effects on flame speed propagation. *Energy Conversion and Management*, *308*, 118395. https://doi.org/10.1016/j.enconman.2024.118395

Bhaduri, S., & Mallikarjuna, J. M. (2023). Comparison of Performance and Emission Characteristics of a Gasoline Engine with Laser and Spark Ignitions in Partially Stratified Mode—A Computational Fluid Dynamics Analysis. *SAE International Journal of Engines*, *16*(3), 377-398. https://www.jstor.org/stable/27349141

Biçer, B., & Yurtkuran, A. (2020). Parameter and design analysis for gasoline direct injection injector using CFD and design of experiments. *Journal of Applied Fluid Mechanics, 13*(1), 119-132. https://doi.org/10.29252/jafm.13.01.29896

Booker, A. J., Dennis, J. E., Frank, P. D., Serafini, D. B., Torczon, V., & Trosset, M. W. (1999). A rigorous framework for optimization of expensive functions by surrogates. *Structural Optimization, 17*, 1-13. https://doi.org/10.1007/BF01197708

Bora, B. J., Dai, T. T., Shadangi, K. P., Sharma, P., Said Z., Kalita, P., Buradi, A., N, H., Pham, M. T., & Le, C. T. (2022). Improving combustion and emission characteristics of a biogas/biodiesel-powered dual-fuel diesel engine through trade-off analysis of operation parameters using response surface methodology. *Sustainable Energy Technologies and Assessments, 53*, 102455. https://doi.org/10.1016/j.seta.2022.102455

Bredberg, J. (2001). On two-equation eddy-viscosity models. *Department of Thermo and Fluid Dynamics, Chalmers University of Technology, Göteborg, Sweden*.

Cecere, G., Irimescu, A., & Merola, S. (2023). Design of an Optically Accessible Intake Manifold for Characterization of Liquid and Gaseous Jets in PFI Operating Conditions. *Design, 7*(1), 24. https://doi.org/10.3390/designs7010024

Clerc, S. (2000). Numerical simulation of the homogeneous equilibrium model for two-phase flows. *Journal of Computational Physics, 161*(1), 354-375. https://doi.org/10.1006/jcph.2000.6515

Czitrom, V. (1999). One-factor-at-a-time versus designed experiments. *The American Statistician, 53*(2), 126-131. https://doi.org/10.1080/00031305.1999.10474445

Forte, C., Bianchi, G. M., & Corti, E. (2012). *Multicycle simulation of the mixture formation process of a PFI gasoline engine.* SAE Technical Paper. https://doi.org/10.4271/2011-01-2463

Gammaidoni, T., Miliozzi, A., Zembi, J., & Battistoni, M. (2024). Hydrogen mixing and combustion in an SI internal combustion engine: CFD evaluation of premixed and DI strategies. *Case Studies in Thermal Engineering*, *55*, 104072. https://doi.org/10.1016/j.csite.2024.104072

Ghasemi, A., Shams, M., & Heyhat, M. M. (2017). A numerical scheme for optimizing gas liquid cylindrical cyclone separator. *Journal of Process Mechanical Engineering, 231*(4), 836-848. https://doi.org/10.1177/0954408916644002

Giancarlo, A. (2009). Reynolds-averaged Navier--Stokes equations for turbulence modeling. *Applied Mechanics Reviews, 62*(4). https://doi.org/10.1115/1.3124648

Golzari, R., Li, Y., & Zhao, H. (2016). *Impact of port fuel injection and in-cylinder fuel injection strategies on gasoline engine emissions and fuel economy.* SAE Technical Paper. https://doi.org/10.4271/2016-01-2174

Hellmann, R., Jochmann, P., Leick, P., Stapf, K. G., Schünemann, E., & Thévenin, D. (2018). *Multi-Objective optimization of high-pressure gasoline injector nozzles using Genetic Algorithm coupled with Computational Fluid Dynamics (CFD): exploiting the manufactural design space.* 14th ICLASS.

Hellmann, R., Jochmann, P., Stapf, K. G., Schuenemann, E., Daróczy, L., & Thévenin, D. (2017). *Towards design optimization of high-pressure gasoline injectors using Genetic Algorithm coupled with Computational Fluid Dynamics (CFD).* Ilass Europe. 28th European conference on Liquid Atomization and Spray Systems (pp 880-887). Editorial Universitat Politècnica de València. http://doi.org/10.4995/ILASS2017.2017.4586

Hinckel, J. N., Nova, H. V., & Bazarov, V. G. (2008). *CFD analysis of swirl atomizers.* 44th AIAA/ASME/SAE/ASEE Joint Propulsion Conference and Exhibit.

Holland, J. H. (1992). *Adaptation in natural and artificial systems: an introductory analysis with applications to biology, control, and artificial intelligence.* MIT press.

Kalghatgi, G. T. (2015). Developments in internal combustion engines and implications for combustion science and future transport fuels. *Proceedings of the Combustion Institute, 35*(1), 101-115. https://doi.org/10.1016/j.proci.2014.10.002

Maio, G., Boberic, A., Giarracca, L., Aubagnac-Karkar, D., Colin, O., Duffour, F., Deppenkemper, K., Virnich, L., & Pischinger, S. (2022). Experimental and numerical investigation of a direct injection spark ignition hydrogen engine for heavy-duty applications. *International Journal of Hydrogen Energy, 47*(67), 29069-29084. https://doi.org/10.1016/j.ijhydene.2022.06.184

Menter, F. R. (1994). Two-equation eddy-viscosity turbulence models for engineering applications. *AIAA Journal, 32*(8), 1598-1605. https://doi.org/10.2514/3.12149

Menter, F. R., Lechner, R., & Matyushenko, A. (2019). Best practice: generalized k-ω two-equation turbulence model in ANSYS CFD (GEKO). *ANSYS Germany GmbH, 107*, 108. https://www.ansys.com/content/dam/amp/2022/march/quick-request/Best-Practice-GEKO-Turbulence-Modeling-in-Ansys-CFD.pdf

Menter, F. R., Matyushenko, A., & Lechner, R. (2020). *Development of a generalized k-ω two-equation turbulence model.* New Results in Numerical and Experimental Fluid Mechanics XII: Contributions to the 21st STAB/DGLR Symposium (pp. 101-109). Darmstadt, Germany: Springer. https://doi.org/10.1007/978-3-030-25253-3_10

Mohammadi, B., & Pironneau, O. (1993). *Analysis of the k-epsilon turbulence model.*

Most, T., & Will, J. (2008). Metamodel of optimal prognosis-an automatic approach for variable reduction and optimal metamodel selection. *Proc. Weimarer Optimierungs-und Stochastiktage, 5*, 20-21. https://doi.org/10.13140/2.1.2194.4007

Most, T., & Will, J. (2010). Recent advances in Meta-model of Optimal Prognosis. *Proceedings of the Weimar Optimization and Stochastic Days, 7*(21), 10-22. https://doi.org/10.13140/2.1.3374.0488

Most, T., & Will, J. (2011). ensitivity analysis using the Metamodel of Optimal Prognosis. *Weimar Optimization and Stochastic Days, 8*. https://doi.org/10.48550/arXiv.2408.03590

Nouri-Borujerdi, A., & Kebriaee, A. (2012). Numerical simulation of laminar and turbulent two-phase flow in pressure-swirl atomizers. *AIAA Journal, 50*(10), 2091-2101. https://doi.org/10.2514/1.J051331

Pan, M., Shu, G., Wei, H., Zhu, T., Liang, Y., & Liu, C. (2014). Effects of EGR, compression ratio and boost pressure on cyclic variation of PFI gasoline engine at WOT operation. *Applied Thermal Engineering, 64*(1-2), 491-498. https://doi.org/10.1016/j.applthermaleng.2013.11.013

Ptchelintsev, A., Grewolls, G., Will, J., & Theman, M. (2010). *Applying sensitivity analysis and robustness evaluation in virtual prototyping on product level using optislang.* SIMULIA Customer Conference. Citeseer. https://library.dynardo.de/fileadmin/Material_Dynardo/bibliothek/RDO/SCC2010-nokia_final.pdf

Rashid, A. N. M. H. N., Hairuddin, A. A., Rezali, K. A. M., Masuri, S. U., Jaafar, J., & Fitriyana, D. F. (2024). Computational Fluid Dynamics (CFD) Validation and Investigation the Effect of Piston Bowl Geometries Performance on Port Fuel Injection-Homogeneous Charge Compression Ignition (PFI-HCCI) Engines. *Journal of Advanced Research in Numerical Heat Transfer, 18*(1), 30-48. https://doi.org/10.37934/arnht.18.1.3048

Rațiu, S. (2003). The history of the internal combustion engine. *Annals of the Faculty of Engineering Hunedoara, 1*, 145-148. https://annals.fih.upt.ro/pdf-full/2003/ANNALS-2003-3-21.pdf

Reitz, R. D. (2013). Directions in internal combustion engine research. *Combustion and Flame , 160*(1), 1-6. https://doi.org/10.1016/j.combustflame.2012.11.002

Relich, M. (2016). Computational intelligence for estimating cost of new product development. *Foundations of Management, 8*(1), 21-34. https://doi.org/10.1515/fman-2016-0002

Robert, B. (2022). *Bosch automotive handbook.* Willey.

Sagdeev, D. I., Fomina, M. G., Mukhamedzyanov, G. K., & Abdulagatov, I. M. (2013). Experimental study of the density and viscosity of-heptane at temperatures from 298 K to 470 K and pressure upto 245 MPa. *International Journal of Thermophysics, 34*(1), 1-33. https://doi.org/10.1007/s10765-012-1373-z

Sahoo, S., & Srivastava, D. K. (2023). Numerical analysis of performance, combustion, and emission characteristics of PFI gasoline, PFI CNG, and DI CNG engine. *Energy*, 278, 127749. https://doi.org/10.1016/j.energy.2023.127749

Salim, S. M., & Cheong, C. S. (2009). Wall Y strategy for dealing with wall-bounded turbulent flows. *Proceedings of the International Multiconference of Engineers and Computer Scientists*, 2, 2165-2170. https://www.iaeng.org/publication/IMECS2009/IMECS2009_pp2165-2170.pdf

Schmidt, D. P., Nouar, I., Senecal, P. K., Rutland, C., Martin, J., Reitz, R. D., & Hoffman, J. A. (1999). Pressure-swirl atomization in the near field. *SAE Transactions*, 471-484. http://www.jstor.org/stable/44743386

Serra, N. (2023). Revisiting RANS turbulence modelling used in built-environment CFD simulations. *Building and Environment, 237*, 110333. https://doi.org/10.1016/j.buildenv.2023.110333

Singh, I., Güdden, A., Raut, A., Dhongde, A., Emran, A., Sharma, V., & Wagh, S. (2024). Experimental and numerical investigation of a single-cylinder methanol port-fuel injected spark ignition engine for heavy-duty applications. *SAE Technical Paper*, *14*. https://doi.org/10.4271/2024-26-0072

Smil, V. (2005). *Creating the twentieth century: Technical innovations of 1867-1914 and their lasting impact*. Oxford University Press. https://doi.org/10.1093/0195168747.001.0001

Vikhar, P. A. (2016). *Evolutionary algorithms: A critical review and its future prospects*. International Conference on Global Trends in Signal Processing, Information Computing and Communication (pp. 261-265). IEEE. https://doi.org/10.1109/ICGTSPICC.2016.7955308

Wang, X., Zhao, H., & Xie, H. (2016). Effect of dilution strategies and direct injection ratios on stratified flame ignition (SFI) hybrid combustion in a PFI/DI gasoline engine. *Applied Energy, 165*, 801-814. https://doi.org/10.1016/j.apenergy.2015.12.116

Wilcox, D. C. (2008). Formulation of the kw turbulence model revisited. *AIAA Journal, 46*(11), 2823-2838. https://doi.org/10.2514/1.36541

Yago, G. (1983). The sociology of transportation. *Annual Review of Sociology*, *9*(1), 171-190. https://doi.org/10.1146/annurev.so.09.080183.001131

Yang, J., Kaiser, E. W., Siegl, W. O., & Anderson, R. W. (1993). *Effects of port-injection timing and fuel droplet size on total and speciated exhaust hydrocarbon emissions.* SAE Technical Paper. https://doi.org/10.4271/930711

Yusuf, S. N., Asako, Y., Sidik, N. A., Mohamed, S. B., & Japar, W. M. (2020). A short review on rans turbulence models. *CFD Letters, 12*(11), 83-96. https://doi.org/10.37934/cfdl.12.11.8396

Zoumpourlos, K., Coraddu, A., Geertsma, R., & Ketterij, R. V. D. (2023). Evaluation of methanol sprays in marine internal combustion engines: a case study for port fuel injection systems. *Modelling and Optimisation of Ship Energy Systems*. https://doi.org/10.59490/moses.2023.655

APPENDIX I: GEKO TURBULENCE MODEL

The GEKO turbulence model of steady flow can be expressed as follows (Menter et al., 2019),

$$\frac{\partial(\rho U_j k)}{\partial x_j} = P_k - C_\mu \rho k \omega + \frac{\partial}{\partial x_j}\left[\left(\mu + \frac{\mu_t}{\sigma_k}\right)\frac{\partial k}{\partial x_j}\right], \quad (8)$$

and

Table 7 Definition and the range of six free parameters for GEKO turbulence model including their default value (Menter et al., 2019)

Parameter	Definition	Range	Default
C_{SEP}	Optimize the separation prediction for boundary layer	[0.7,2.5]	1.75
C_{NW}	Optimize the wall shear stress and wall heat transfer rates in non-equilibrium flows	[-2.0,2.0]	0.50
C_{MIX}	Optimize the mixing spreading rates in free shear flows	[0.0,1.0]	C_{MIXCOR}
C_{JET}	Optimize the spreading rates of jet flows	[0.0,1.0]	0.90
C_{CORNER}	Optimize the secondary flows in corners	[0.0,1.5]	1.00
C_{CURV}	Optimize the curvature correction	[0.0,1.5]	1.00

$$\frac{\partial(\rho U_j \omega)}{\partial x_j} = C_{\omega 1} F_1 \frac{\omega}{k} P_k - C_{\omega 2} F_2 \rho \omega^2 + \rho F_3 CD + \frac{\partial}{\partial x_j}\left[\left(\mu + \frac{\mu_t}{\sigma_\omega}\right)\frac{\partial \omega}{\partial x_j}\right], \quad (9)$$

with

$$\mu_t = \rho v_t = \rho \frac{k}{\max\left(\omega, \frac{S}{C_{Realize}}\right)}, \quad (10)$$

$$P_k = \tau_{ij}\frac{\partial U_i}{\partial x_j}, \quad (11)$$

$$\tau_{ij}^{EV} = -\rho \overline{u_i' u_j'} = 2\mu_t S_{ij} - \frac{2}{3}\rho k \delta_{ij}, \quad (12)$$

$$CD = \frac{2}{\sigma_\omega}\frac{1}{\omega}\frac{\partial k}{\partial x_j}\frac{\partial \omega}{\partial x_j}, \quad (13)$$

$$\tau_{ij} = \tau_{ij}^{EV} - C_{CORNER}\frac{1.2\mu_t}{max\left(0.3\omega\sqrt{0.5(S^2+\Omega^2)}\right)}\left(S_{ik}\Omega_{kj} - \Omega_{ik}S_{kj}\right), \quad (14)$$
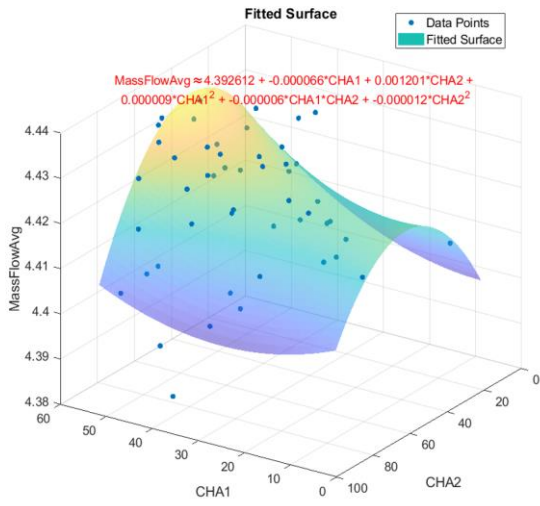
with

$$S_{ij} = \left(\frac{\partial U_i}{\partial x_j} + \frac{\partial U_j}{\partial x_i}\right), \Omega_{ij} = \frac{1}{2}\left(\frac{\partial U_i}{\partial x_j} - \frac{\partial U_j}{\partial x_i}\right) \quad (15,16)$$
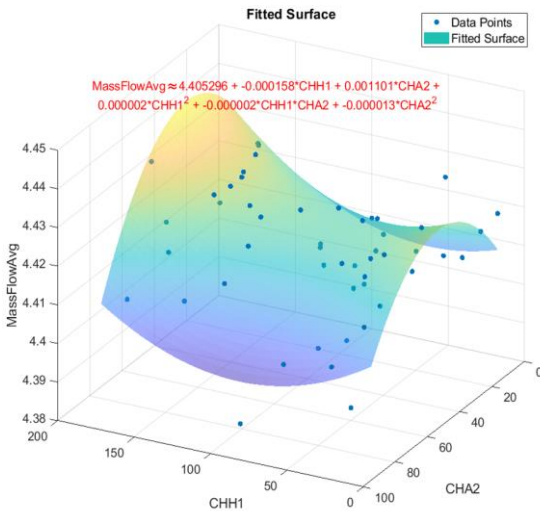
where

$$S = \sqrt{2S_{ij}S_{ij}}, \Omega = \sqrt{2\Omega_{ij}\Omega_{ij}}. \quad (17,18)$$

The GEKO turbulence model provides the six free parameters listed in Table 7 for adjusting the flow according to their applications without negatively impacting the model (Yusuf et al., 2020). The C_{MIXCOR} as

(a)

(b)

Fig. 11 Approximated expression functions of (a) CHA1 (°) and CHA2 (°) vs. MassFlowAvg (kg/h) (b) CHH1 (μm) and CHA2 (°) vs. MassFlowAvg (kg/h)

the default value for C_{MIX} in Table 7 can be expressed as (Menter et al., 2019, 2020),

$$C_{MIXCOR} = 0.35 sign(C_{SEP} - 1)\sqrt{(|C_{SEP} - 1|)}. \tag{19}$$

Note that the default GEKO model using all six defaults for their free parameters performs closely to the Shear Stress Transport (SST) turbulence model (Menter et al., 2019).
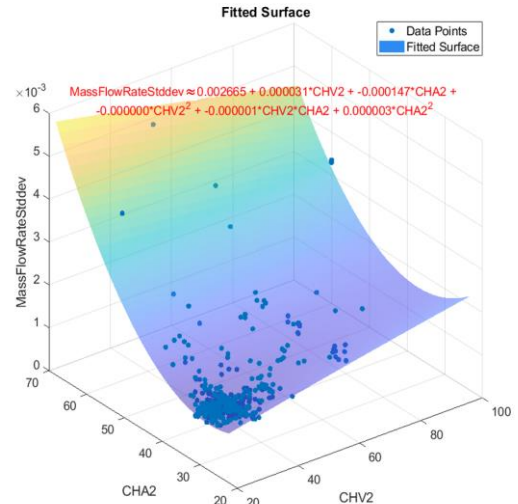
APPENDIX II: SURFACE FUNCTION EXPRESSION

Figure 11 graphically show the fitted 3D surfaces of the all 49 averaged mass flow rate data points as an approximation obtained by using MATLAB. Here, the MassFlowAvg (in kg/h) is a 3D surface function of CHA1

(°) and CHA2 (°) in Fig. 11(a) as well as of CHH1 (μm)
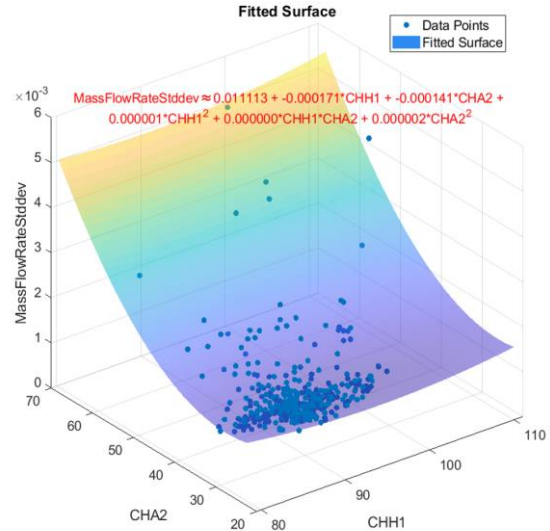
(a)

(b)

Fig. 12 Approximated function expression of (a) CHH1 (μm) and CHA2 (°) vs. MassFlowRateStddev (kg/h) (b) CHV2 (μm) and CHA2 (°) vs. MassFlowRateStddev (kg/h)

and CHA2 (°) in Fig.11(b), with the expressions, as follows:

$$
\begin{aligned}
MassFlowAvg \approx\ & 4.39 - 6.60 \times 10^{-5} CHA1 \\
& + 1.20 \times 10^{-3} CHA2 \\
& + 9 \times 10^{-6} CHA1^2 \\
& - 6 \times 10^{-6} CHA1 \cdot CHA2 \\
& - 1.2 \times 10^{-5} CHA2^2
\end{aligned} \tag{19}
$$

$$
\begin{aligned}
MassFlowAvg \approx\ & 4.41 - 1.58 \times 10^{-5} CHH1 \\
& + 1.10 \times 10^{-3} CHA2 \\
& + 2 \times 10^{-6} CHH1^2 \\
& - 2 \times 10^{-6} CHH1 \cdot CHA2 \\
& - 1.3 \times 10^{-5} CHA2^2
\end{aligned} \tag{20}
$$

Similarly, Figs. 12(a) and 12(b) graphically illustrate the fitted 3D surfaces of the the standard deviation of the averaged mass flow rate, MassFlowRateStddev (in kg/h) as a 3D surface function of CHA2 (°) and CHH1 (μm) as well as of CHV2 (μm) and CHA2 (°), respectively, with the expressions, as follows:

Table 8 Range of the 4 design parameters used for samples in experiment and simulation

	Parameter	Lower bound	Upper bound
Upper edges (for all cases)	CHA1 (°)	37.00	45.00
	CHH1 (μm)	51.74	131.00
Original range (Nominal)	CHA2 (°)	50.85	75.55
	CHV2 (μm)	38.48	65.58
Small bottom edge	CHA2 (°)	37.23	64.40
	CHV2 (μm)	14.00	48.00
Large bottom edge	CHA2 (°)	51.03	57.33
	CHV2 (μm)	59.00	92.00

$$\text{MassFlowRateStddev}$$
$$\approx 0.01 - 1.71 \times 10^{-4}\text{CHH1}$$
$$- 1.41 \times 10^{-4}\text{CHA2} \qquad (21)$$
$$+ 1 \times 10^{-6}\text{CHH1}^2$$
$$+ 2 \times 10^{-6}\text{CHA2}^2$$

$$\text{MassFlowRateStddev}$$
$$\approx 2.67 \times 10^{-3}$$
$$+ 3.1 \times 10^{-5}\text{CHV2}$$
$$- 1.47 \times 10^{-4}\text{CHA2} \qquad (22)$$
$$- 1 \times 10^{-6}\text{CHV2} \cdot \text{CHA2}$$
$$+ 3 \times 10^{-6}\text{CHA2}^2$$

The specific function expressions for each fitted surface as an approximation obtained by using MATLAB are shown on top of each 3D surface in red.

APPENDIX III: VALIDATION

The available experimental data were brought into consideration to qualitatively validate the simulation results. The experimental data were obtained by varying the bottom edge defined by the two design parameters, namely CHV2 and CHA2. The 353 valve seats for each of the following 3 cases with the different ranges of CHV2 and CHA2 were designed, produced, and tested:

Case 1: Original range (Nominal)

Case 2: Small bottom edge - limiting CHV2 and CHA2 values to be smaller compared to the original range.

Case 3: Large bottom edge - Increasing CHV2 and CHA2 values to be larger than those of the original range.

Due to production limitation, the upper edge defined by the two design parameters, namely CHA1 and CHH1, was kept in the same range for all 3 cases. The range of each case is shown in the Table 8.

For each experimental case, all the 353 valve seat samples were produced according to the prescribed
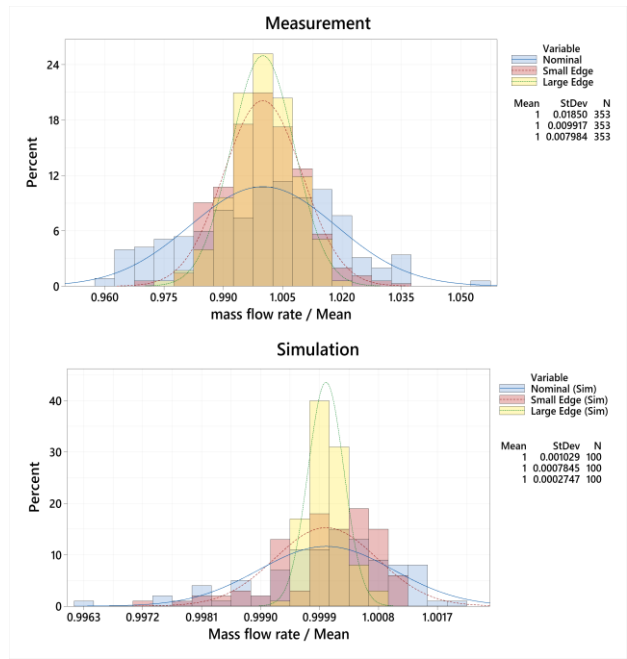

Fig. 13 Standard deviation distribution of the dimensionless mass flow rate in 3 distinctive cases with normal bottom edge, small bottom edge, and large bottom edge for experimental measurement and simulation

dimension listed in the table above and their mass flow rate values were measured. Similarly, their 100 numerical counterparts for each case were randomly generated according to the same values of lower and upper bounds listed in the table above and their mass flow rate values were extracted from the simulation. Note also that some discrepancies between the experimental testing conditions and the simulations may occur, for instance, the tested medium, the uncertainty of the exact geometry from the production line, the error from the measurement. These unavoidable factors could potentially lead to the deviation of the actual mass flow rate measured. Therefore, the most suitable approach to statistically compare the tendency of the mass flow rate is to arrange both measured and simulated mass flow rates into a dimensionless value, i.e., the ratio of the mass flow rate to its averaged mass flow rate (mean value), which are plotted in the Fig. 13.

Figure 13 shows a statistically similar tendency with the highest standard deviation being found in the original range case for both experiment and simulation. An improvement with smaller standard deviation is shown in case of the small bottom edge compared to the original range case. The case of large bottom edge exhibits the best flow behavior in terms of maintaining the lowest standard deviation of the mass flow rate. The experimental cases verify a qualitative validation of the valve seat simulation cases with four design parameters in terms of the mass flow rate or, more specifically, the standard deviation of the mass flow rate, as previously explained in Fig. 9.